Small Structures

small structures

www.small-structures.com

RESEARCH ARTICLE OPEN ACCESS

Photoelectron Spectroscopy of the Phosphorus Monosulfide (PS) and Phosphorus Monoxide (PO) Radicals

Pedro Recio[1] | Jorge Alonso de la Fuente[2] | Myriam Drissi[3] | Niyazi Bulut[4,5] | Jean Christophe Loison[6] | Gustavo Garcia[3] | Susana Gomez Carrasco[7] | Cristina Sanz Sanz[8] | Luis Bañares[1,9] | Sonia Marggi Poullain[1] | Alexandre Zanchet[2]

[1]Departamento de Química Física (Unidad Asociada de I+D+i al CSIC), Facultad de Ciencias Químicas, Universidad Complutense de Madrid, Madrid, Spain | [2]Instituto de Física Fundamental, CSIC, Madrid, Spain | [3]Synchrotron SOLEIL, L'Orme des Merisiers, Gif sur Yvette, France | [4]Department of Physics, Firat University, Elazig, Turkey | [5]Faculty of Applied Physics and Mathematics, Gdańsk University of Technology, Gdańsk, Poland | [6]Institut des Sciences Moléculaires (ISM), CNRS, Univ. Bordeaux, Talence, France | [7]Departamento de Química Física, Facultad de Ciencias Químicas, Universidad de Salamanca, Salamanca, Spain | [8]Departamento de Química Física Aplicada, (Unidad Asociada de I+D+i al CSIC), Facultad de Ciencias, Universidad Autónoma de Madrid, Madrid, Spain | [9]Instituto Madrileño de Estudios Avanzados en Nanociencia (IMDEA Nanoscience), Madrid, Spain

Correspondence: Alexandre Zanchet (alexandre.zanchet@csic.es)

Received: 19 September 2025 | **Revised:** 17 December 2025 | **Accepted:** 5 January 2026

Keywords: astrochemistry | ionization | phosphorus | photoelectron | radicals

ABSTRACT

PO and PS radicals are the smallest units of phosphorus oxides and phosphorus sulfides, respectively, two rich families of refractory compounds widely employed in industrial and technological applications. These two diatomic radicals are also thought to be relevant for the phosphorus (P) chemistry in the interstellar medium (ISM). PO is indeed one of the few P-bearing molecules detected in the ISM, while models also predict a considerable abundance of PS, although its presence in the ISM has not been confirmed yet. Since P is an essential element for the development of life, understanding its relatively unknown chemistry in the ISM is essential for astrobiology. The recent detection of PO^+ in surprisingly high abundance in the ISM also suggests that the cations are likely to be relevant too for the ISM chemistry of phosphorus. While PO and PO^+ are relatively well known, experimental data available in the literature for PS are very scarce and its cation PS^+ is mainly unknown spectroscopically, hindering its possible detection in the ISM. In this work, we present slow photoelectron spectra of both species generated in situ in a discharge flow reactor. From these spectra, and with the support of electronic structure calculations, we have determined the adiabatic ionization energy of both radicals ($IE_{PO} = 8.377 \pm 0.006$ eV, $IE_{PS} = 7.904 \pm 0.006$ eV) and the spin–orbit splitting of the $^2\Pi$ ground state of PS ($350 \pm 34\,cm^{-1}$). We also show that in the case of PO, the splitting is smaller than $250\,cm^{-1}$. In addition, relevant information on the vibrational structure of the two cationic ground states is extracted, providing useful spectroscopic data on the two species which might contribute to the ISM detection of these species, their vibrational bands falling within the spectral coverage of the James Webb Space Telescope (JWST).

1 | Introduction

Phosphorus (P) is one of the main biogenic elements, as it is present in all known life forms, including nucleic acids and nucleotides, while is relevant in several metabolic functions [1]. With a low relative abundance of 2.8×10^{-7} relative to H in the solar atmosphere [2], it can be assumed that this biogenic relevance was not determined by the cosmic abundance of P, but rather by its particular bonding properties significantly influenced by the 3*d* orbitals which permit coordination numbers of 1, 3, 4, 5, and 6 [1]. On Earth, P presents, however, a higher relative abundance than in space.

Phosphorus exhibits indeed a high propensity to form refractory materials such as phosphates, which are ubiquitous in numerous minerals, and are present in higher concentrations in rocky

planets located close to their stars [1]. Due to its refractory properties, P can be easily locked in grains, explaining why it may be severely depleted from the gas phase in cold regions of the interstellar medium (ISM) and, in particular, along molecule-rich sight lines [3].

It has been demonstrated that a large portion of P may be locked in comet ices in the solar system, mainly in the form of PO [4]. Phosphorus oxides and phosphates are also found in the mineral composition of chondrites, on Earth and Mars, and have been detected in lunar samples and stony-meteorites [5]. While trapped in salts or minerals, it is very unlikely that these species desorb in the gas phase, not only in the ISM but also in a laboratory. Consequently, it is difficult to vaporize them to measure their gas-phase spectroscopy, and despite their relevance for astrobiology, interstellar P chemistry remains relatively unknown [6]. We should also notice that P is the least abundant biogenic element, with relative abundance several orders of magnitude lower than O, C, N, or even S. While huge efforts have been made in recent years to establish phosphorus chemical models in order to explain the observed abundances, the small number of P-bearing molecular species hinders the possibility of establishing reliable constraints on the chemical networks, for which many routes are still unexplored [7, 8]. For now, only few P-bearing species have been detected in the ISM: PN [9, 10], PO [11], PO^+ [8], CP [12], SiP [13], HCP [14], CCP [15], and PH_3 [16, 17], mostly in circumstellar shells or star-forming regions.

A clear example is the case of the phosphorus monosulfide (PS). Models predict that PS is expected to be as abundant as PO in Asymptotic Giant Branch (AGB) atmospheres [18]. The spectroscopy of PS has been, however, scarcely investigated experimentally [19–24], and its photoelectron spectrum (PES) has not been measured, although some calculations are available in the literature [25]. In contrast, several experimental studies have been reported for PO, establishing most of the PO and PO^+ diatomic constants [19, 26–39]. Nevertheless, some discrepancies are found in the determination of the ionization energy of PO, and the latest determination was recommended in early 2000 [40].

In addition to their astrochemical interest, PO and PS are the smallest species of phosphorus oxides and sulfides, respectively. Phosphorus oxides and sulfides are characterized by the formation of a rich variety of stable clusters of the type P_nX_m (X = O, S). They may grow by polymerization and can easily combine with metals or carbon nanotubes to form a vast and chemically-versatile family of materials [41]. These properties make phosphorus oxides and sulfides interesting materials for technological applications in the fields of semiconductors [42], nanomaterials for medical applications [43], catalysis [44], or energy storage [45], among others. Studying the spectroscopy of PO and PS radicals will help to characterize the chemical properties of their bonding, a fundamental knowledge that may bring new insights to deepen our understanding on the rich, yet not fully understood, chemistry of phosphorus.

In this work, we present the first slow photoelectron spectrum (SPES) of PS^+ and revisit the one of PO^+ by taking advantage of the photoion-photoelectron coincidence (PEPICO) spectrometer DELICIOUS III [46], available at DESIRS beamline of the synchrotron SOLEIL [47]. The experimental set-up includes a discharge flow-tube to generate the desired radicals [48]. The results allow us the determination of the adiabatic ionization energies (AIEs) of both species and provide information on the vibrational structure of their cations. In addition, these spectra provide information on the spin–orbit couplings of the neutral species. High-level ab initio calculations for both systems support the experimental results.

2 | Results and Discussion

2.1 | Phosphorus Monosulfide

A mixture of $H_2S + PH_3 + F$ is introduced in the flow-tube so that the F atoms progressively strip H atoms from both H_2S and PH_3. Atomic S and P, as well as SH, PH and PH_2 are produced in the flow-tube and can recombine to produce new species, among them, PS. According to DFT calculations, the PS radical is expected to be formed following the reactions

$$S + PH \rightarrow PS + H \qquad \Delta H = -1.34\,\text{eV} \qquad (1)$$

$$P + SH \rightarrow PS + H \qquad \Delta H = -0.89\,\text{eV} \qquad (2)$$

$$P(^2D) + S_2 \rightarrow PS + S \qquad \Delta H = -1.51\,\text{eV} \qquad (3)$$

Several products are expected in the flow tube, and the concentrations of the different precursors are optimized to maximize the production of PS in the mass spectrum. This is confirmed by the main peak appearing at $m/z = 63$ in TOFMS integrated between 7.5 and 9 eV photon energy presented in Figure 1. Peaks at other m/z are also observed, although with a remarkably lower intensity. The $m/z = 64$ can be assigned to either S_2^+, HPS^+ or probably both. This was, however, no further investigated, being out of the scope of this work. The $m/z = 65$ is attributed to the second most abundant isotope of sulfur, $P^{34}S^+$, since its area with

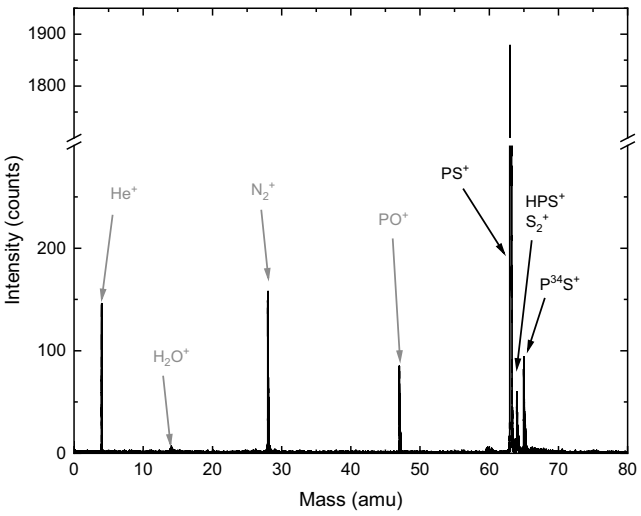

FIGURE 1 | Time-of-flight mass spectrum (TOFMS) obtained from the integration of the photoionization of the species generated by using a mixture of H_2S+PH_3+F in the 7.5–9.0 eV photon energy range. PS^+ and HPS^+ are visible at $m/z = 63$ and 64, respectively. At $m/z = 65$, the signal of $P^{34}S$ is observed. Peaks at $m/z = 4$ and 28, are due to the carrier gases He^+ and N_2^+. The signal at $m/z = 47$ is attributed to PO^+ after the reaction PH + O when adding a small leak of O_2 in the discharge flow-tube.

respect to PS is consistent with the relative abundance of ^{34}S of 4.4%. In addition, the peak observed at $m/z = 47$ can be attributed to PO^+, likely produced by atomic O introduced by an air leak in the discharge, which can react with PH_3 to produce PO. Even if the O_2 leak is small, the reaction $O + PH_3$ is known to be very efficient [49]. Finally, two peaks at $m/z = 4$ and $m/z = 28$ correspond to the carrier gases He and N_2, which are the dominant species in the mixture, and may be ionized by the remaining higher order harmonics of the synchrotron radiation that are not absorbed by the Ar gas filter. Other expected species formed in the flow-tube do not appear in the TOFMS due to their higher ionization potential (>9 eV).

The mass-selected SPES of PS is presented in Figure 2, while the corresponding photoionization matrix from which it was extracted, by selecting photoelectrons with kinetic energies lower than 20 meV, is shown in Figure SM2 of the Supplementary Material. The spectrum consists of a series of structures separated by about 0.1 eV. Their intensity decreases with increasing photon energy, and they can be attributed to the photoionization of PS into the first vibrational levels of PS^+ in its ground electronic state.

The potential energy curves (PECs), computed for PS^+ in several electronic states, are presented in Figure 3, and confirm that only the ground state of the cation is accessible by photon energies lower than 9 eV. The most intense peak in Figure 2 is tentatively assigned to the photoionization of PS($X\,^2\Pi_{1/2}$, $\nu = 0$) into PS^+($X\,^1\Sigma^+$, $\nu' = 0$), while ν'>0 are assigned consecutively to the series of highest peaks appearing for increasing photon energy.

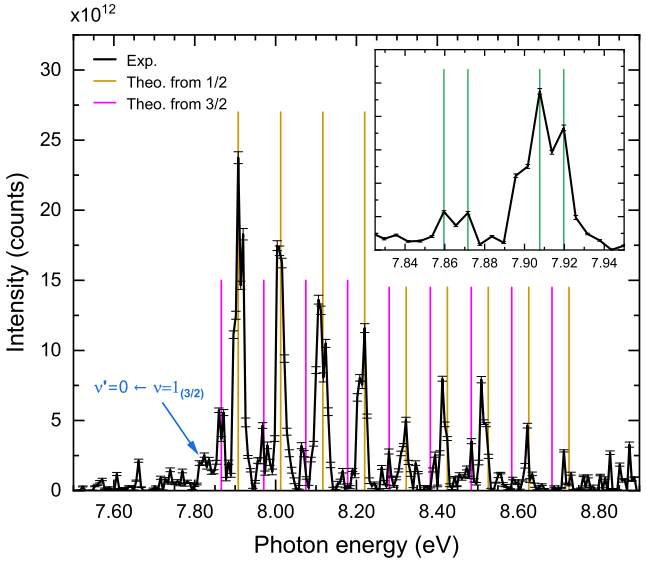

FIGURE 2 | Experimental slow photoelectron spectrum (SPES) recorded for PS (black line). Dark yellow vertical lines show the expected positions for the photoionization from PS($X\,^2\Pi_{1/2}$)($\nu = 0$) into the PS^+ ground state in consecutive ν' levels. Magenta vertical lines indicate the respective position for PS($X\,^2\Pi_{3/2}$)($\nu = 0$), based on RCCSD(T) calculations. The small peak at lower photon energies is assigned to the photoionization from $\nu = 1$ into $\nu = 0$ of the respective electronic ground states, as indicated in blue. The expanded view in the inset (top right) shows the splitting of the two first peaks assigned to the generation of PS in both $\nu = 0$ and $\nu = 1$ (see text for details).

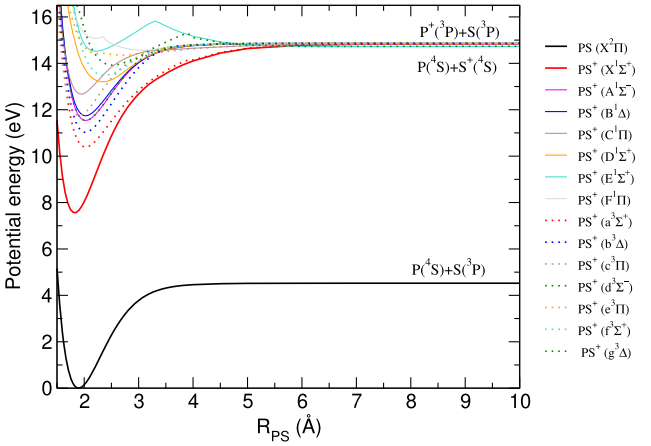

FIGURE 3 | MRCI + Q/V5Z potential energy curves of PS ground electronic state and all the singlet and triplet electronic states of PS^+ correlating to $P^+(^3P)$+$S(^3P)$ and $P(^4S)$+$S^+(^4S)$. For clarity, the triplet states are represented with dashed lines.

Additionally, satellite peaks of lower intensity can be distinguished to the left of each intense peak (see Figure 2), i.e., at lower photon energies. They are located about 0.04 eV ($350 \pm 34\ cm^{-1}$) lower in energy than the main peaks in the spectrum. These satellites are associated to the photoionization from the spin–orbit excited state of PS($X^2\Pi_{3/2}$). Since the PS^+ cation exhibits a $^1\Sigma^+$ character, it presents only one spin–orbit component. Therefore, ionization from both $^2\Pi_{1/2}$ and $^2\Pi_{3/2}$ neutral states will lead to the same electronic state of the cation. As a consequence, the spin–orbit excited state of neutral PS will present a lower ionization threshold, which is reflected in the SPES as a satellite peak shifted by the spin–orbit splitting energy.

It is worth noticing that most of the peaks in Figure 2 appear as doublets, with both peaks of comparable intensities, as observed in the expanded view in the inset. The spectral step employed does not allow us to extract precise values, but the doublet nature can be clearly observed with an approximate separation of 0.012 eV ($\approx 100\ cm^{-1}$) in all peaks. This value is quite close to $110\ cm^{-1}$, the difference between $E_{\nu=1} - E_{\nu=0}$ of PS ($733.7\ cm^{-1}$ [50]) and $E_{\nu'=1} - E_{\nu'=0}$ of PS^+ ($843.6\ cm^{-1}$, calculated from the potential energy curves presented in this work as it will be discussed later in the text). Transition $\nu' = 0 \leftarrow \nu = 0$ and the sequence band $\nu' = 1 \leftarrow \nu = 1$ are thus expected to exhibit a shift of this magnitude. The doublet feature of comparable intensity seems to indicate a population of $\nu = 1$ comparable to the one of ν=0 of the neutral radical generated in the flow-tube. The presence of signal below 7.8 eV on the SPES (see Figure 2), which is too large to be attributed to noise, can only be attributed to hot bands, showing that higher ν may also be populated, but in much lower proportion. Otherwise the doublet nature of the peaks would not be observed. The main carrier gas, He, is indeed known to be efficient for thermalization of molecular rotation, but not as effective to thermalize vibration. A significant population of $\nu = 1$ is therefore not surprising giving the exothermicity of Equations (1)-(3).

Since the splitting of the peaks is not fully resolved, there is a small uncertainty regarding the energy position of each structure in the SPES. In order to confirm the proposed assignment, the doublet feature was ignored in the procedure, and each band

has been fitted to a Gaussian function to extract its center. The energy position is represented as a function of $\nu' + \frac{1}{2}$ and fitted to a second degree polynomial function. The result is depicted in Figure S3.

The first order term corresponds to the harmonic frequency (ω_e) and the second order term to the anharmonicity ($\omega_e\chi_e$). Following this procedure, the adiabatic ionization energy (AIE) can be derived as the position of the first band. The obtained AIE (7.904 ± 0.006) is consistent with the position of the most intense peak of the SPES (7.908 ± 0.003), supporting further the assignment. In addition to the AIE, a vibrational harmonic frequency of $\omega_e = 841 \pm 40$ cm^{-1} and a remarkably low value of χ_e (0.004 cm^{-1}) are found, indicating that the PEC of the PS^+ ground state is nearly harmonic, at least for the first vibrational levels. As a consequence, the derived value of χ_e shows a large relative error and should only be considered as an approximate value.

From a theoretical point of view, the energy difference between the neutral and cation ground states minima, depicted in Figure 3, is calculated to be 7.55 eV without accounting for spin–orbit couplings. This value is obtained by fitting the respective PECs to extract their exact equilibrium position. Even considering the corrections for spin–orbit coupling and both zero-point energies (ZPE), the MRCI ionization potential is found to be much lower than the experimental determination of 7.904 eV. It is expected though that the MRCI method underestimates the ionization potential, in part due to the self-consistency error inherent to the method. However, such a large deviation seems to indicate that the MRCI method, with the active space considered here, cannot recover all the electronic correlation energy, which seem to be important in the PS bonding. Thus, probably a larger active space would provide better results. This result is consistent with the findings of Yaghlane and co-workers [25], who found a similar ionization energy of 7.57 eV, also using a MRCI method.

To obtain more accurate values, instead of increasing the active space, which would lead to a considerable increase of the computational resources, we have calculated the PECs for both ground states of PS and PS^+ in the Franck–Condon region, using the RCCSD(T) method. The theoretical AIE value of 7.873 eV matches reasonably well the experimental data (neither accounting for spin–orbit couplings nor for ZPE differences).

To improve further the theoretical estimation of the AIE, the spin–orbit contribution and the ZPE corrections have to be considered. The theoretical spin–orbit splitting of the neutral ground state arising from our calculation is found to be 325.6 cm^{-1} near the equilibrium position, slightly larger than the value derived from rotational lines and smaller, but still within the error bar, than the value derived from the SPES of PS^+ (350 ± 34 cm^{-1}). Considering this value for the spin–orbit splitting of PS($X\ ^2\Pi$) and a difference of 110 cm^{-1} in harmonic frequencies (corresponding to a 55 cm^{-1} difference in ZPE), a first order correction of 0.027 eV can be made to estimate the effective AIE, which is found to be 7.900 eV, in very good agreement with the experimental data.

By fitting the PECs to a Morse function, a first approximation of the harmonic frequency and the anharmonicity can be obtained and compared with their respective experimental values. The obtained results are shown in Table 1 together with the experimental data, as well as reported values already discussed above.

TABLE 1 | Ionization energy (IE), spin–orbit splitting (SO) and equilibrium distance of PS($X\ ^2\Pi$), and spectroscopic constants of PS^+($X\ ^1\Sigma^+$), obtained in this work and the comparison with previous works. The method of assignment is indicated in parenthesis. MRCI and RCCSD(T) refer to theoretical calculations, SPES refers to experimental values derived from the slow photoelectron spectra. "Rotational" refers to values derived experimentally from the spacing of rotational lines and EXOMOL refers to the values considered in the EXOMOL spectroscopic database.

PS($X\ ^2\Pi$)		
	This work	**Other works**
IE (eV)	7.904 ± 0.006 (SPES)	7.571 (MRCI) [25]
	7.556 (MRCI)	7.888 (RCCSD(T)) [25]
	7.873 (RCCSD(T))	
	7.900 (RCCSD(T) + SOC + ZPE)	
SO (cm^{-1})	350 ± 34 (SPES)	321.93 (Rotational) [21]
	325.6 (MRCI)	320.8 (Rotational) [22]
		321.74 (Rotational) [23]
		291.4 (MRCI) [25]
		327.0 (MRCI) [51]
r_e (Å)	1.8976 (MRCI)	1.898 (Rotational) [23]
	1.8979 (RCCSD(T))	1.9 (Rotational) [22]
		1.8977 (EXOMOL) [50]
		1.904 (MRCI) [51]
		1.879 (MRCI) [25]
PS^+($X\ ^1\Sigma^+$)		
	This work	**Other works**
r_e (Å)	1.8242 (MRCI)	1.829 (MRCI) [25]
	1.8280 (RCCSD(T))	1.8269 (MRCI) [52]
		1.872 (CI) [53]
ω_e (cm^{-1})	841 ± 40 (SPES)	839 (MRCI) [25]
	854 (MRCI)	852 (MRCI) [52]
	848 (RCCSD(T))	838 (CI) [53]
$\omega_e\chi_e$ (cm^{-1})	3.3 (MRCI)	3.13 (MRCI) [25]
	3.2 (RCCSD(T))	3.273 (MRCI) [52]
Rot. B (cm^{-1})	0.321986 (MRCI)	0.31720 (MRCI) [25]
	0.320633 (RCCSD(T))	0.3213 (MRCI) [52]

As it can be appreciated, a good agreement is found between theory and experiment, and all the values compare well with findings of other works, validating the procedure employed for the assignment of the SPES.

By knowing the electronic potentials, it is also possible to solve the nuclear Schrödinger equation to compute the exact vibrational levels, without relying on an approximate method consisting in fitting the curves to a Morse potential. To do so, we

TABLE 2 | Experimentally derived and calculated vibrational levels of PS^+. For comparison, the experimental values are obtained by resting the derived AIE to the position of the bands of the SPES, while the theoretical values are obtained by resting the calculated energy of $\nu' = 0$. Vibrational energies are given in cm^{-1}. All the experimental values show an estimated error of $40\,cm^{-1}$.

ν'	SPES	RCCSD(T)	MRCI
0	0.0	0.0	0.0
1	841	843.5567	846.9539
2	1639	1682.1289	1687.7236
3	2451	2514.5108	2522.0890
4	3278	3339.5567	3349.9007
5	4074	4157.2642	4171.2021
6	4853	4968.4714	4986.1258
7	5736	5774.1017	5794.7616
8	6470	6574.8887	6597.2256
9		7371.0203	7393.5228

employed the program DUO [54] to calculate the vibrational levels. The energies of the first 10 vibrational levels were computed using both MRCI and RCCSD(T) PECs, and the obtained vibrational levels are given in Table 2.

The differences in vibrational energies obtained with the two potentials is rather small, less than $4\,cm^{-1}$ for $\nu' = 1$ and around $20\,cm^{-1}$ for $\nu' = 9$. The theoretical vibrational energies compare well with the experimental values with a similar energy difference for $\nu' = 1$ and around $100\,cm^{-1}$ for $\nu' = 8$.

This means that if the MRCI energies of the cation are rescaled to the correct ionization energy, the vibrational progression up to $v = 7$ is well reproduced by MRCI calculations, with tiny differences compared to RCCSD(T), and both agree well with the experimental vibrational bands. We can thus conclude that the calculations are trustworthy to determine the PECs, even if the relative energies between neutral and cation are slightly underestimated in the case of MRCI. Vertical bars are included in Figure 2 showing the expected position based on RCCSD(T) calculations for the photoionization from $PS(X\,^2\Pi_{1/2}, \nu = 0)$ into $PS^+(X\,^1\Sigma^+, \nu')$ (magenta lines) and $PS(X\,^2\Pi_{3/2}, \nu = 0)$ into $PS^+(X\,^1\Sigma^+, \nu')$ (dark yellow lines). The good agreement between theory and experiment also validates the procedure employed to assign the different bands.

2.2 | Phosphorus Monoxide

Although, as seen in Figure 1, PO was detected when using the previous mixture ($F + H_2S + PH_3$) together with a small air leak in the gas line of the discharge, its production was maximized by using pure O_2 through the discharge, to create a mixture of atomic oxygen and phosphine, which is known to be very efficient [49].

The reaction is triggered by

$$O + PH_3 \rightarrow H + H_2PO \qquad \Delta H = -1.02\,eV \qquad (4)$$

followed sequentially by

$$O + H_2PO \rightarrow OH + HPO \qquad \Delta H = -2.34\,eV \qquad (5)$$

and

$$O + HPO \rightarrow OH + PO \qquad \Delta H = -1.60\,eV \qquad (6)$$

Other products such as H_3PO, PO_2, and HPO_2 are also expected to be formed, but in much lower quantities [49].

As previously, the respective concentrations of reactants and reaction time were optimized to maximize the signal of PO^+. The TOFMS obtained from photoionization in the 8.0–8.9 eV photon energy range using the PH_3+O mixture is shown in Figure 4. The TOFMS exhibits an intense peak at $m/z = 47$ corresponding to PO^+, as well as two smaller peaks at $m/z = 48$ and $m/z = 49$, assigned to HPO^+ and H_2PO^+, respectively. No peak attributable to H_3PO is observed under our experimental conditions. The peaks associated with the carrier gases He and N_2 are similarly observed.

The SPES for PO is shown in Figure 5, while the corresponding photoionization matrix from which it was extracted is shown in Figure SM5 of the Supplementary Material. Three clear bands of decreasing intensity are observed and are assigned to the photoionization of PO into the three first vibrational levels of PO^+ in its ground electronic state. The assignment is supported by the PECs of PO and PO^+ depicted in Figure 6, which shows, similarly to the PS radical, that only the ground state of the cation is accessible with photon energies lower than 8.8 eV. As expected, the PECs of PO and PS cations are very similar to each other and to neutral CO, which is isoelectronic in the valence shell with the two cations, leading to a characteristic triple bond. The only remarkable difference between the sets of curves of PO^+ and PS^+ is the dissociation channel leading to neutral atomic phosphorus. While in the case of PS^+, this channel is very close in energy to those leading to neutral atomic sulfur, in the case of PO^+, the channel leading to oxygen cation is considerably higher

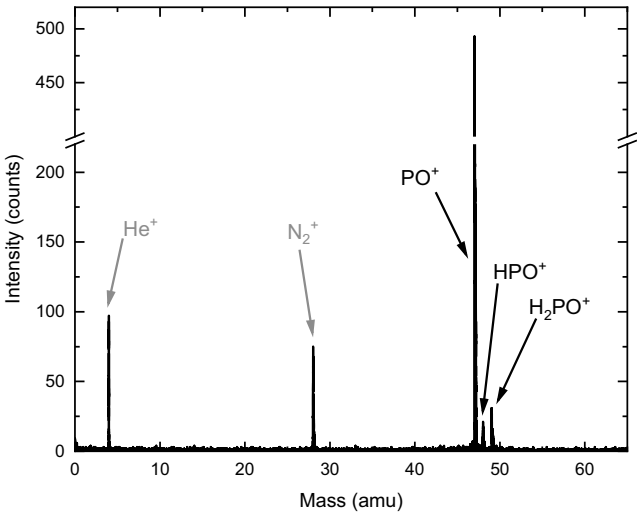

FIGURE 4 | TOFMS obtained from the integration of the photoionization in the 8.0–8.9 eV photon energy range using the PH_3 + O mixture. PO^+, HPO^+ and HPO_2^+ are visible at m/z = 47, 48 and 49, respectively. The peaks at m/z = 4 and 28, correspond to He^+ and N_2^+, respectively, used as carrier gases in the experiments.

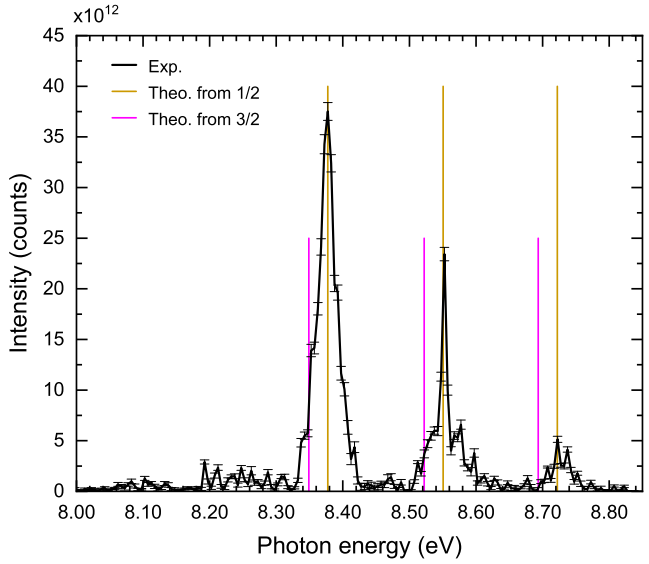

FIGURE 5 | Experimental SPES recorded for PO (black line). Dark yellow vertical lines show the expected positions for the photoionization from PO($X\ ^2\Pi_{1/2}$)($\nu = 0$) into the PO^+ ground state in consecutive ν' levels, while magenta vertical lines indicate the respective positions from PO($X\ ^2\Pi_{3/2}$)($\nu = 0$) based on RCCSD(T) calculations.

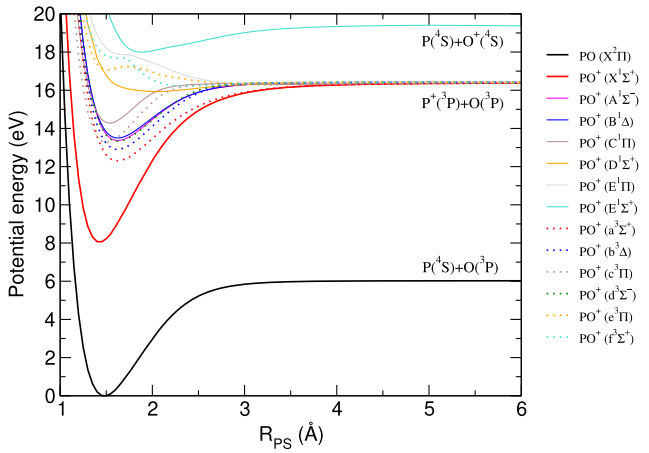

FIGURE 6 | MRCI + Q/V5Z potential energy curves (PECs) of PO ground electronic state and all the singlet and triplet electronic states of PO^+ correlating to $P^+(^3P) + O(^3P)$ and $P(^4S) + O^+(^4S)$. For clarity, the triplet states are represented with dashed lines.

in energy. This is due to the fact that S and P present similar ionization potentials of 10.36 eV and 10.49 eV, respectively, while the ionization potential of atomic O is about 13.62 eV.

Concerning the bands observed in the SPES of PO, they are much broader in contrast with the SPES of PS, and only three peaks are observed, matching pretty well the observations of Dyke and coworkers [35]. The signature of the spin–orbit splitting of the $X\ ^2\Pi$ state of PO is indeed not resolved since only shoulders can be seen in the spectrum, and, at variance with PS, no splitting due the generation of PO($\nu = 1$) is observed.

Considering the estimated resolution of the experiment, it would have been expected to observe at least the spin–orbit satellite peak. However, this is hindered by spectroscopic congestion leading to broad bands. This broadening, also observed in the experiment of Dyke and coworkers [35], reflects contributions of the sequence bands and spin–orbit components, explaining also the shoulders observed to the right of the first band. It is therefore challenging to accurately determine the energies of the rovibronic transitions. Nevertheless we have attempted so by fitting Gaussian functions to the observed bands to estimate the vibrational progression ($\nu = 0 \rightarrow \nu' = n$).

The first band in the SPES shown in Figure 5 is assigned to photoionization from PO($X\ ^2\Pi_{1/2,3/2}, \nu = 0$) into $PO^+(X\ ^1\Sigma^+, \nu' = 0)$, and the two other peaks are consequently attributed to $\nu' = 1$ and 2. The energy position of the three peaks has been represented as a function of $\nu' + \frac{1}{2}$ and fitted to a second degree polynomial function, as depicted in Figure SM6 of the Supplementary Material. As only three peaks are observed, the anharmonicity, which seems to be negligible, was not extracted. The first order gives a vibrational frequency of $1419 \pm 70\ cm^{-1}$, in agreement, with the reported frequency by Dyke and coworkers [35] of $1410\ cm^{-1}$. The AIE obtained from the polynomial fitting is 8.377 ± 0.006 eV, and matches the most intense peak position. This value agrees well with that reported by Dyke et al. [35], 8.39 ± 0.01 eV, and by Ghosh and Verma [33], 8.373 eV, or Verma et al. [55], 8.38 eV.

From a theoretical point of view, the ionization energy extracted from the MRCI PECs presented in Figure 6 is 8.06 eV. As in the case of PS, the MRCI calculation using the present active space does not seem to capture properly all the electronic correlation energy to provide a reliable estimation of the ionization threshold, which is clearly underestimated. To improve the theoretical estimation, RCCSD(T) calculations were similarly performed for PO and PO^+ ground states. The energy difference between the two minima is found to be 8.344 eV. At equilibrium position, the calculated spin–orbit splitting of PO($X\ ^2\Pi$) is $235\ cm^{-1}$. Vertical bars in Figure 5 show the calculated positions for the photoionization from PO($X\ ^2\Pi_{1/2}, \nu = 0$) into $PO^+(X\ ^1\Sigma^+, \nu')$ (dark yellow lines) and PO($X\ ^2\Pi_{3/2}, \nu = 0$) into $PO^+(X\ ^1\Sigma^+, \nu')$ (magenta lines). As it can be seen in Figure 5, the magenta lines match pretty well the position of the shoulder of the peak. The later was employed by Dyke et al. [35] to estimate the spin–orbit splitting of PO ($240\ cm^{-1}$), value that matches pretty well. From our results, we can only argue that the splitting has to be lower than $250\ cm^{-1}$, else we would have observed it as a peak, and not as a shoulder.

The ZPE of PO^+ ground state is calculated at $704\ cm^{-1}$ and $705\ cm^{-1}$ with MRCI and RCCSD(T) methods, respectively, while the ZPE of PO is estimated at $610\ cm^{-1}$ by Prajapat and coworkers [50]. Considering the purely electronic RCCSD(T) ionization energy and accounting for spin orbit and ZPE correction, the refined theoretical estimation of the ionization threshold is found to be 8.37 eV, in close agreement with experimental values. All the derived data are summarized and compared in Table 3.

As stated previously, the theoretical harmonic frequencies and anharmonicity are obtained by fitting the potential energy curves to a Morse potential. To obtain more accurate values, we computed the exact vibrational levels associated to the MRCI and RCCSD(T) potentials from this work. They are presented in Table 4. As for PS^+, only small differences are found for the energies of the first nine vibrational levels, with less than $2\ cm^{-1}$ for

TABLE 3 | AIE and spin–orbit (SO) splitting for PO($X\ ^2\Pi$) and spectroscopic constants PO^+($X\ ^1\Sigma^+$).

PO		
	This work	**Other works**
IE (eV)	8.377 ± 0.003 (SPES)	8.39 (He I PES) [35]
	8.370 (RCCSD(T)+ ZPE + SO)	8.373 (Rydberg Series) [33]
	8.06 (MRCI + Q)	8.38 (IR emission) [55]
	8.344 (RCCSD(T))	8.36 (RCCSD(T)) [40]
SO (cm^{-1})	<250 (SPES)	224 (rotational) [37]
	235 (MRCI)	240 (He I PES) [35]
		218 (MRCI) [56]
		213 (MRCI) [50]
		224 (EXOMOL) [50]
r_e (Å)	1.4800 (MRCI)	1.4756 (Rotational) [57]
	1.4776 (RCCSD(T))	1.4865 (RCCSD(T)) [40]
		1.4741 (MRCI) [56]
PO^+		
	This work	**Other works**
r_e (Å)	1.4278 (MRCI)	1.4250 (Rotational) [58]
	1.4268 (RCCSD(T))	1.4262 (MRCI) [59]
		1.4347 (RCCSD(T)) [40]
ω_e (cm^{-1})	1419 ± 70 (SPES)	1411 (Rotational) [58]
	1412 (MRCI)	1410 (He I PES) [35]
	1413 (RCCSD(T))	1412 (MRCI) [59]
		1401 (RCCSD(T)) [40]
$\omega_e\chi_e$ (cm^{-1})	7.3 (MRCI)	7.11 (Rotational) [58]
	7.2 (RCCSD(T))	10 (He I PES) [35]
		7.53 (MRCI) [59]
Rot. B (cm^{-1})	0.78396 (MRCI)	0.78435 (Rotational) [58]
	0.78507 (RCCSD(T))	0.7856 (MRCI) [59]

the relative energy of $\nu' = 1$ and around 20 cm^{-1} for $\nu' = 9$. These values fall within the error bar of the experimental one for the first two vibrational levels, with less than 20 cm^{-1} difference in energy for $\nu' = 1$ and less than 10 cm^{-1} for $\nu' = 2$.

3 | Conclusion

The slow photoelectron spectra of phosphorus monosulfide (PS) and phosphorus monoxide (PO) have been reported up to 9 eV photon energy using a double imaging photoelectron-photoion spectrometer in conjunction with synchrotron radiation. PS was produced by successive H-atom abstractions of two precursors, phosphine and hydrogen sulfide, which can further react in a flow tube reactor. PO was produced in the flow tube by the $O + PH_3$ reaction. With the support of accurate ab initio calculations, the assignment of the different bands of the spectra allowed us to determine some spectroscopic constants for both radical and respective cations ground electronic states. In particular, the threshold ionization of PO and PS radicals as well as their spin–orbit splitting could be measured, and the vibrational spectroscopic constants of PS^+ and PO^+ could be determined.

TABLE 4 | Experimentally derived and calculated vibrational levels of PO^+. For comparison, the experimental values are obtained by resting the derived AIE to the position of the bands of the SPES while the theoretical values are obtained by resting the calculated energy of $\nu' = 0$. Vibrational level energies are given in cm^{-1}. All the experimental values show an estimated error of 70 cm^{-1}.

ν'	**SPES**	**RCCSD(T)**	**MRCI**
0	0.0	0.0	0.0
1	1416	1398.4253	1396.5988
2	2786	2783.2737	2779.1671
3		4154.3506	4147.7546
4		5511.4135	5502.3768
5		6854.3874	6843.0215
6		8183.4653	8169.8476
7		9498.6190	9482.6824
8		10 800.0508	10 781.6008
9		12 087.8615	12 066.6188

It is interesting to note that both PO and PS exhibit relatively low threshold ionization energies of 8.377 and 7.904 respectively, compared with the ionization energies of the constituting atoms, P, S and O, which all present ionization energies larger than 10 eV. This is not the case for phosphorus hydrides and fluorides, which are expected to form in the flow tube, but are not observed in the TOFMS at 9 eV photon energy, while the hydroxide cations HPO^+ and H_2PO^+ do appear in the TOFMS. The relatively low ionization energy of PO probably explains in part the surprisingly large PO^+/PO ratio observed in the ISM, and a similar situation is expected for PS, which presents an even lower ionization energy. This lowering of the ionization energy seems thus to be attributable to the PO and PS bonding for which $d-$orbitals play an important role. This is supported by the discrepancy observed between the MRCI (without including these orbitals in the active space) and the RCCSD(T) ionization energy. To confirm this hypothesis, a MRCI calculation including the *d*-orbitals in the active space have been performed on PO and PO^+ ground states with a smaller basis set, AVTZ. In this case, as it can be appreciated in Figure SM7 of the supplementary material, the difference in energy between the two minima is 8.37 eV, instead of 8.06 eV when $d-$orbitals are not included in the active space. Despite the use of a smaller basis set, this value is in much closer agreement with the RCCSD(T) value (8.34 eV), thus confirming the relevance of $d-$orbitals in the PO and PO^+ bonding. It is worth to remark that, while the inclusion of $d-$orbitals in the active space improves the determination of the IE, the reduction of the size of the basis set (required to perform the calculation) leads to a displacement of the PECs toward larger distances and a

change of their curvature. The sensitivity of the results on those parameters provides an additional clue on the importance of electronic correlation in the PO bonding. Unfortunately, a similar calculation cannot be performed for PS, since it would require additionally the inclusion of $d-$orbitals of the sulfur atom, making the calculation unaffordable, even with small basis sets. Nevertheless, the results obtained with PO suggest that $d-$orbitals will also play an important role in the PS bonding. This particularity in the PO and PS bonding provides also a hint on why larger phosphorus oxides and sulfides can form a large variety of stable clusters which can easily polymerize.

It is also interesting to point out the ease with which these species condense, at least at 300 K. In both experiments, a relatively fast obstruction of the skimmer was indeed observed during the scans, hindering the possibility to reach larger photon energies within the limited beamtime available. This observation gives an additional clue that most of the elemental phosphorus in the ISM may be locked in grains, not only in form of hydrides, but more likely in the form of oxides and sulfides. The observed ease of condensation of these species present (PO) or expected to be present (PS) in circumstellar envelopes also suggests that they may play a role in the formation of the primordial grains, expected to form in these regions of the ISM. Further experimental studies, in particular at higher temperatures, will therefore be necessary to confirm the validity of this hypothesis.

4 | Methods

4.1 | Experimental

The experiments are performed using the double imaging photoelectron/photoion coincidence i2PEPICO spectrometer DELICIOUS III [47] located in the permanent end-station SAPHIRS [60] at the DESIRS beamline of synchrotron SOLEIL [46]. PS and PO radicals are generated in situ by combining different precursors in a flow-tube reactor. The set-up is described elsewhere [48], and has been used as an efficient and reliable way to produce small refractory species in the gas phase, such as SiC [61] or SiS [62]. Fluorine atoms, produced by microwave discharge of F_2 (Air liquide 5% in He) are fed into the reactor where the precursors H_2S (Air liquide 99.5%) and PH_3 (1.5% in N_2) are injected. The fluorine atoms react with the hydrides and strip the H-atoms. The resulting radicals may then recombine to form a variety of species, among them, PS. The best signal was obtain with a total pressure of 3.0×10^{-1} mbar in the reactor for a total flow of around 1000 sccm (standard cubic centimeter per minute). The concentrations of atomic F, PH_3 and H_2S are measured to be around 1×10^{14}, 2×10^{13}, and 4×10^{13} cm^{-3}, respectively.

The relatively high abundance of atomic F is necessary to provide several abstraction reactions on PH_3 and H_2S in order to optimize PS production (through P + SH and S + PH reactions). The distance between the end of the injector and the end of the reactor was adjusted to optimize PS production, leading to a reaction time equal to 4 ms. Similarly to PS, for the generation of PO radicals, a mixture of PH_3 (1.5% in N_2) and atomic O, produced by microwave discharge of molecular O_2, are employed.

At the center of the DELICIOUS III spectrometer, the synchrotron radiation intersects the molecular beam at a right angle. Electrons and ions generated from this interaction are extracted and accelerated in opposite directions by a continuous electric field. Electrons are detected using velocity map imaging (VMI), while ions are analyzed with a modified Wiley–McLaren time-of-flight (TOF) imaging spectrometer. Electron/ion pairs are temporally correlated within the coincidence scheme, so that photoelectron images can be filtered by cation mass. In addition, because of the net velocity in the molecular beam direction, events can be filtered by the position of arrival of the cation, so that only species originating in the reactor are considered, notably increasing the signal-to-background ratio [48].

Detailed energy scans were recorded for PS^+ and PO^+ in the photon energy ranges of 7.5–8.9 and 8.0–8.9 eV, respectively, with a step size of 6 meV. At each photon energy, ion mass- and position-selected photoelectron spectra (PES) are derived from the respective electron VMI images by Abel transformation 63]], leading to the so-called photoionization matrix, which represents the number of events for a given mass as a function of electron and photon energies. These matrices are reduced to extract the slow photoelectron spectra (SPES), as detailed elsewhere [64], which yield the cation spectroscopy with a good resolution/signal compromise. The calibration of the spectra were performed using the signal of He^+. All the spectra have been corrected by the synchrotron photon flux. Additionally, the smooth signal decay observed in some of the scans due to skimmer clogging, is also corrected by comparison to fast and lower resolution scans (100 meV steps), 7.5–9.5 eV for PS^+ and 8.0–11.0 eV for PO^+ energy ranges (Figures S1 and S4), carried out first in both cases. It was necessary since in both experiments, condensation of unidentified refractory materials on the skimmer, e.g., either phosphorus oxides/sulfides polymers or salts, lead to the complete obstruction of the skimmer, allowing us only reduced acquisition time.

Synchrotron radiation from an undulator is dispersed using a 6.65-meter normal incidence monochromator equipped with a 200 lines/mm grating. A gas filter containing argon is employed to suppress high-order harmonics from the undulator, ensuring spectral purity. The contents of the flow-tube reactor are collimated using two sequential skimmers (Beam Dynamics, 2.0 mm diameter) leading to a mild adiabatic expansion. The overall resolution must take into account the resolutions of the photons and electrons energies, respectively. The photon energy is fixed by the monochromator slits, which Ar adjusted to achieve a photon energy resolution of $\approx$ 8 meV. Meanwhile, the electron energy resolution depends on the measurement conditions and is estimated to be 13 meV, in the present case. The convolution of both lead to a overall resolution of 15 meV. The minimum error in the measurements is given by half of the spectral step employed in the scans, which corresponds to an error of 3 meV ($\approx 25\ cm^{-1}$). For the AIE of both PS and PO, the error is estimated to be 0.006 eV, the half-width of the fitted gaussians. For the frequencies and associated quantitites, the error is given by the polynomial fit.

4.2 | Theoretical

The electronic structure calculations to determine the potential energy curves (PECs) of PO, PS, and their respective cations are performed using the MOLPRO 2022 package [65]. The full PECs

of the ground state of both radicals, and all the singlet and triplet electronic states of their cations, correlating to $P^+(^3P)$+X(^3P) and P(^4S)+X(^4S), with (X = O, S), are computed using the MRCI method [66] with Davidson correction [67]. The MRCI wave function is built using the orbitals generated at SA-CASSCF level [68] and considering an active space of 6 (cations) and 7 electrons (neutral) in 6 orbitals, the three valence *p*-orbitals of both atoms. Within the $C2_v$ symmetry, the first $^2B_1$ and $^2B_2$ states (the two components of the $^2\Pi$ ground state) of the neutral radical together with all the states of the cation correlating to the atomic fragments in their ground states are included. This corresponds to four A_1 states, two B_1 states, two B_2 states, and two A_2 states for each singlet, triplet and quintuplet spin multiplicities. The inclusion of all these states allows a good description of the nondynamical correlation in the asymptotic regions where most of the electronic states of the cation become degenerated, and well behaved orbitals along all the PECs. By analogy with NO radical, it is in principle expected that the PX bonding (X = S, O) will form through the valence *s* and *p* – orbitals of both atoms. Consequently, the active space is increased by including the valence *s*-orbital of two atoms at the MRCI level. Both 1*s* orbitals are however kept frozen since they are not expected to play a role neither in the bonding nor in the ionization energy. It is worth to point out that P and S atoms also possess *d* – orbitals in their valence shell, and ideally, including them in the active space would improve further the description. However, the number of configurations arising from this larger active space increases drastically, with a huge impact on the computational cost. In the case of PO, calculations wih few electronic states are still feasible by reducing the size of the basis set. However, in the case of PS which requires five additional *d* – orbitals compared with PO, the number of configurations explodes making the calculation untractable. The quintuplet states are not computed at the MRCI level. To determine the spin–orbit splitting of the radical ground states, the spin–orbit couplings between $^2B_1$ and $^2B_2$ states have been computed using the Breit–Pauli operator, within the scheme implemented in MOLPRO [69]. The cc-pV5Z basis set is employed for the MRCI calculations providing the complete set of potential energy curves.

In addition, the PECs of the ground states of the PO and PS radicals and their respective cations are also computed at the RCCSD(T) level of theory. As in the case of the MRCI calculations, only the 1*s* orbitals are kept frozen in order to capture properly the core-valence correlation. Mono-reference methods are known to not be able to describe properly bond breaking, thus the RCCSD(T) calculations were restricted to the Franck–Condon region, which are within the [1.1–1.9] Å interval for PO and [1.6–2.3] Å interval for PS. RCCSD(T) calculations are done with the aug-cc-pwCVQZ basis set. To explore the impact of the inclusion of *d* – orbitals in the active space, the same calculation was performed at MRCI level with increased active space in the case of PO. This heavier calculation was done using the aug-cc-pVTZ basis set.

To obtain more accurate description of the vibrational levels of the ground state of the cations, the ab initio points (MRCI or RCCSD(T)), sampled over the PECs, are interpolated by cubic splines and are employed to solve the nuclear motion variationally. The first ten vibrational levels for a $^1\Sigma^+$ state are calculated using the DUO program [54].

Finally, the exothermicities of the reactions (1)–(6) are calculated at the DFT level using the M06-2X functional and AVTZ basis set with Gaussian16 [70].

Author Contributions

Alexandre Zanchet: conceptualization (lead), data curation (equal), writing – original draft (lead). **Pedro Recio:** data curation (lead), writing – original draft (equal). **Jorge Alonso de la Fuente:** data curation (equal), writing – original draft (supporting). **Sonia Marggi Poullain:** conceptualization (supporting), data curation (equal), writing –original draft (equal). **Myriam Drissi:** data curation (equal), writing – original draft (supporting). **Gustavo Garcia:** conceptualization (supporting), data curation (equal), writing – original draft (supporting). **Niyazi Bulut:** data curation (equal), writing – original draft (supporting). **Jean Christophe Loison:** data curation (equal), writing – original draft (supporting). **Susana Gomez Carrasco:** data curation (equal), writing – original draft (supporting). **Cristina Sanz Sanz:** data curation (equal), writing – original draft (supporting). **Luis Bañares:** conceptualization (supporting), data curation (equal), writing – original draft (supporting).

Acknowledgements

The authors acknowledge the COST Action CA21101 (COSY) for support and facilitating collaborations. This research was carried out within the Unidad Asociada Química Física Molecular between the Departamento de Química Física of Universidad Complutense de Madrid and CSIC. This work has received financial support from European Union, the French "Agence Nationale de la Recherche" (ANR) under grant no. ANR-21-CE29-0017 (Project ZEPHIRS) and from MCIN (Spain) under grant PID2021-122549NB-C21, PID2021-122549NB-C22, PID2021-122839NB-I00, PID2023-147215NB-I00, PID2024-155352NB-C21, and PID2024-155352NB-C22. This work was partially funded by the regional government of Madrid (Spain) through the Tecnologías 2024 program, project MATRIX-CM (grant no. TEC-2024/TEC-85). This work was performed on the DESIRS beamline at the SOLEIL synchrotron under proposal no. 20241287. They are grateful to the whole staff at SOLEIL for smoothly running the facility, in particular the beamline staff and Jean–François Gil for his precious help in performing the experiments. They also acknowledge the computing time on HPC DRAGO (CSIC). P.R. gratefully acknowledges financial support through the Juan de la Cierva program of the Spanish Ministry of Science, Innovation and Universities. N.B. is grateful for the support provided by the Nobelium programme "Joining Gdańsk Tech Research Community," under grant number DEC-1/12025/IDUB/I.1a/No: 038122.

Funding

This work was supported by the Ministerio de Asuntos Económicos y Transformación Digital, Gobierno de España (PID2021-122549NB-C21, PID2021-122549NB-C22, PID2021-122839NB-I00, PID2023-147215NB-I00, PID2024-155352NB-C21 and PID2024-155352NB-C22), Agence Nationale de la Recherche (ANR-21-CE29-0017), and COST Action (CA21101).

Conflicts of Interest

The authors declare no conflicts of interest.

Data Availability Statement

The data that support the findings of this study are available from the corresponding author upon reasonable request.

References

1. E. Macia, "The Role of Phosphorus in Chemical Evolution," *Chemical Society Reviews* 34 (2005): 691.

2. N. Grevesse and A. J. Sauval, "Standard Solar Composition," *Space Science Reviews* 85 (1998): 161.

3. P. Aschenbrenner, K. Butler, and N. Przybilla, "The Present-Day Cosmic Phosphorus Abundance," *A& A* 698 (2025): A164.

4. V. M. Rivilla, M. N. Drozdovskaya, K. Altwegg, et al., "Alma and Rosina Detections of Phosphorus-Bearing Molecules: The Interstellar Thread between Star-Forming Regions and Comets," *Monthly Notices of the Royal Astronomical Society* 492 (2020): 1180.

5. E. Macia, M. V. Hernandez, and J. Oro, "Primary Sources of Phosphorus and Phosphates in Chemical Evolution," *Origins of Life and Evolution of the Biosphere : the Journal of the International Society for the Study of the Origin of Life* 27 (1997): 459.

6. F. Fontani, "Observations of Phosphorus-Bearing Molecules in the Interstellar Medium," *Frontiers in Astronomy and Space Sciences* 11 (2024): 1451127.

7. J. Chantzos, V. M. Rivilla, A. Vasyunin, et al., "The First Steps of Interstellar Phosphorus Chemistry," *A& A* 633 (2020): A54.

8. V. M. Rivilla, J. G. de la Concepcion, I. Jimenez-Serra, et al., "Ionize Hard: Interstellar PO^+ Detection," *Frontiers in Astronomy and Space Sciences* 9 (2022): 829288.

9. B. E. Turner and J. Bally, "Detection of Interstellar PN: The First Phosphorus Compound in the Interstellar Medium," *The Astrophysical Journal* 321 (1987): L75.

10. L. M. Ziurys, "Detection of Interstellar PN: The First Phosphorus-Bearing Species Observed in Molecular Clouds," *The Astrophysical Journal* 321 (1987): L81.

11. E. D. Tenenbaum, N. J. Woolf, and L. M. Ziurys, "Identification of Phosphorus Monoxide ($X^2\pi$) in VY Canis Majoris: Detection of the Forst P-O Bond in Space," *The Astrophysical Journal* 666 (2007): L29.

12. M. Guelin, J. Cernicharo, J. Paubert, and B. E. Turner, "Free Cp in Irc+10216," *A& A* 230 (1990): L9.

13. L. A. Koelemay, M. A. Burton, A. P. Singh, P. M. Sheridan, J. J. Bernal, and L. M. Ziurys, "Laboratory and Astronomical Detection of the Sip Radical ($x^2\pi_i$): More Circumstellar Phosphorus," *The Astrophysical Journal Letters* 940 (2022): L11.

14. M. Agundez, J. Cernicharo, and M. Guelin, "Discovery of Phosphaethyne (HCP) in Space: Phosphorus Chemistry in Circumstellar Envelopes," *The Astrophysical Journal* 662 (2007): L91.

15. D. T. Halfen, D. J. Clouthier, and L. M. Ziurys, "Detection of the CCP Radical ($x^2\pi_r$) in Irc+10216: A New Interstellar Phosphorus-Containing Species," *The Astrophysical Journal* 677 (2008): L101.

16. M. Agundez, J. Cernicharo, J. R. Pardo, M. Guelin, and T. G. Philips, "Tentative Detection of Phosphine in Irc+10216," *A& A* 485 (2008): L33.

17. E. D. Tenenbaum and L. M. Ziurys, "A Search for Phosphine in Circumstellar Envelopes: PH_3 in Irc+10216 and Crl 2688?," *The Astrophysical Journal* 680 (2008): L121.

18. M. Agundez, J. I. Martinez, P. L. de Andres, J. Cernicharo, and J. A. Martin-Gago, "Chemical Equilibrium in AGB Atmospheres: Successes, Failures, and Prospects for Small Molecules, Clusters, and Condensates," *A& A* 637 (2020): A59.

19. K. Dressler, "Ultraviolett und Schumannspektren der neutralen und ioisierten Molekule PO, PS, NS, P2," *Helvetica Physica Acta* 28 (1955): 563.

20. J. Drowart, C. E. Meyers, R. Szwarc, A. Vandereau, and O. Uy, "Dissociation-Energies of Molecules PS, PSE, and PTE," *High Temperature Science* 5 (1973): 482.

21. A. Janouvrier and B. Pascat, "Le spectre électronique de ps. première partie : le système $d^2\pi - x^2\pi$," *Canadian Journal of Physics* 56 (1978): 1088.

22. T. K. Balasubramanian, M. N. Dixit, and N. A. Narasimham, "Rotational Analysis of the Ultraviolet Bands of PS," *Pramana – Journal of Physics* 12 (1979): 707.

23. K. Kawaguchi, E. Hirota, M. Ohishi, et al., "Infrared Diode Laser Spectroscopy of the PS Radical," *Journal of Molecular Spectroscopy* 130 (1988): 81.

24. H. Klein, E. Klisch, and G. Winnewisser, "Rotational Spectra of Phosphorus Monosulfide up to 1 THz," *Zeitschrift für Naturforschung A* 54 (1999): 137.

25. S. B. Yaghlane, J. S. Francisco, and M. Hochlaf, "Accurate Theoretical Study of PS^q (q = 0,+1,-1) in the Gas Phase," *The Journal of Chemical Physics* 136 (2012): 244309.

26. K. S. Rao, "Rotational Analysis of the γ System of the Po Molecule," *Canadian Journal of Physics* 36 (1958): 1526.

27. N. A. Narasimham, M. N. Dixit, and V. Sethuraman, "$^2\sigma^- \rightarrow x^2\pi$ Band System of Po," *Proceedings of the Indian Academy of Sciences* 62 (1965): 314.

28. R. D. Verma and M. N. Dixit, "The D and D' States of the PO Molecule," *Canadian Journal of Physics* 46 (2079): p.

29. M. N. Dixit and N. A. Narasimham, "Isotope Shift Studies of the Ultra-Violet and Visible Bands of $P^{16}O$ and $P^{18}O$," *Proceedings of the Indian Academy of Sciences* 68 (1968): 1.

30. J. Drowart, C. E. Myers, R. Szwarc, A. V. Auwera-Mahieu, and O. M. Uy, "Determination by the Mass Spectrometric Knudsen Cell Method of the Atomization Energies of the Molecules PO and PO*2*," *Journal of the Chemical Society, Faraday Transactions 2* 68 (1972): 1749.

31. R. D. Verma and S. S. Jois, "Emission Spectrum of the PO Molecule. Part IV. Spectrum in the Region 7000-12000 Å," *Canadian Journal of Physics* 51 (1973): 322.

32. S. Smoes and J. Drowart, "Atomization Energies of Phosphorus Oxides," *Faraday Symposia of the Chemical Society* 8 (1973): 139.

33. S. N. Ghosh and R. D. Verma, "Rydberg States of the PO Molecule," *Journal of Molecular Spectroscopy* 72 (1978): 200.

34. G. Balducci, G. Gigli, and M. Guido, "Dissociation Energies of the Molecules $CrPO_2$(g) and CrO(g) by High-Temperature Mass Spectroscopy," *Journal of the Chemical Society, Faraday Transactions 2* 77 (1981): 1107.

35. J. M. Dyke, A. Morris, and A. Ridha, "Study of the Ground State of PO^+ Using Photoelectron Spectroscopy," *Journal of the Chemical Society, Faraday Transactions 2* 78 (1982): 2077.

36. K. Kawaguchi, S. Saito, and E. Hirota, "Far-Infrared Laser Magnetic Resonance Detection and Microwave Spectroscopy of the PO Radical Available," *The Journal of Chemical Physics* 79 (1983): 629.

37. J. E. Butler, K. Kawaguchi, and E. Hirota, "Infrared Diode Laser Spectroscopy of the PO Radical," *Journal of Molecular Spectroscopy* 101 (1983): 161.

38. S. R. Long, R. C. Sausa, and A. W. Miziolek, "Lif Studies of PO Produced in Excimer Laser Photolysis of Dimethyl Methyl Phosphonate," *Chemical Physics Letters* 117 (1985): 505.

39. K. N. Wong, W. R. Anderson, and A. J. Kotlar, "Radiative Processes following Laser Excitation of the a $^2\sigma^+$ State of PO," *The Journal of Chemical Physics* 85 (1986): 2406.

40. Y. M. O. O. G. R. de Mare, "Properties of the Phosphorus Oxide Radical, PO, Its Cation and Anion in Their Ground Electronic States: Comparison of Theoretical and Experimental Data," *International Reviews in Physical Chemistry* 22 (2003): 641.

41. M. E. Jason, T. Ngo, and S. Rahman, "Products and Mechanisms in the Oxidation of Phosphorus by Sulfur at Low Temperature," *Inorganic Chemistry* 36 (1997): 2633.

42. L. A. Mittmann and A. Crovetto, "Phosphosulfide Semiconductors for Optoelectronics and Solar Energy Conversion," *Journal of Physics: Materials* 7 (2024): 021002.

43. T. Janska, M. Sakmar, M. Stibre, M. Vlk, and J. Kozempel, "Recent Advances in Metal Oxide and Phosphate Nanomaterials Radiolabeling with Medicinal Nuclides," *ACS Omega* 9 (2024): 39297.

44. R. Huang, J. Wang, B. Zhang, K.-H. Wu, Y. Zhang, and D. S. Su, "Phosphorus Oxide Clusters Stabilized by Carbon Nanotubes for Selective Isomerization and Dehydrogenation of β-Isopentene," *Catalysis Science & Technology* 8 (2018): 1522.

45. K. Samdhyan, P. Chand, and H. Anand, "Effective Doping of Phosphorus in Copper Sulfide for High Performance Energy Storage Devices," *Journal of Alloys and Compounds* 936 (2023): 168322.

46. L. Nahon, N. de Oliveira, G. Garcia, et al., "Desirs : A State-of-the-Art VUV Beamline Featuring High Resolution and Variable Polarization for Spectroscopy and Dichroism at SOLEIL," *Journal of Synchrotron Radiation* 19 (2012): 508.

47. G. A. Garcia, B. K. C. de Miranda, M. Tia, S. Daly, and L. Nahon, "Delicious III: A Multipurpose Double Imaging Particle Coincidence Spectrometer for Gas Phase Vacuum Ultraviolet Photodynamics Studies Available," *The Review of Scientific Instruments* 84 (2013): 053112.

48. G. A. Garcia, X. Tang, J.-F. Gil, et al., "Synchrotron-Based Double Imaging Photoelectron/Photoion Coincidence Spectroscopy of Radicals Produced in a Flow Tube: OH and OD," *The Journal of Chemical Physics* 142 (2015): 164201.

49. P. A. Hamilton and T. P. Murrells, "Kinetics and Mechanism of the Reaction of PH_3 with $O(^3P)$ and $N(^4S)$ Atoms," *Journal of the Chemical Society, Faraday Transactions 2* 81 (1985): 1531.

50. L. Prajapat, P. Jagoda, L. Lodi, M. N. Gorman, S. N. Yurchenko, and J. Tennyson, "Exomol Molecular Line Lists – XXIII. Spectra of PO and PS," *Monthly Notices of the Royal Astronomical Society* 472 (2017): 3648.

51. L. Xiao, S. An, D. Liu, B. F. Minaev, H. Agren, and B. Yan, "Absorption Spectra of PS in the Ultraviolet and Infrared Region," *Spectrochimica Acta Part A: Molecular and Biomolecular Spectroscopy* 330 (2025): 125704.

52. H. Liu, D. Shi, J. Sun, and Z. Zhu, "Accurate Spectroscopic Calculations of the 22 Λ-S) States and 60 ω States of PS^+," *Spectrochimica Acta Part A: Molecular and Biomolecular Spectroscopy* 178 (2017): 55.

53. S. P. Karna, P. J. Bruna, and F. Grein, "Electronic States of PS^+ Obtained by Configuration-Interaction Studies," *Chemical Physics* 123 (1988): 85.

54. S. N. Yurchenko, L. Lodi, J. Tennyson, and A. V. Stalyarov, "Duo: A General Program for Calculating Spectra of Diatomic Molecules," *Computer Physics Communications* 202 (2016): 262.

55. R. Verma, M. Dixit, S. Jois, S. Nagaraj, and S. Singhal, "Emission Spectrum of the PO Molecule. Part II. $^2\sigma - {}_2\sigma$ Transitions," *Canadian Journal of Physics* 49 (1971): 3180.

56. H. Liu, D. Shi, J. Sun, and Z. Zhu, "Calculationis on Thirteen Λ-S) States of Po Radical: Electronic Structure, Spectroscopy and Spin–orbit Coupling," *Journal of Quantitative Spectroscopy and Radiative Transfer* 121 (2013): 9.

57. S. Bailleux, M. Bogey, C. Demuynck, Y. Liu, and A. Walters, "Millimeter-Wave Spectroscopy of PO in Excited Vibrational States up to v=7," *Journal of Molecular Spectroscopy* 216 (2002): 465.

58. R. H. Petrmichl, K. A. Petersen, and R. C. Woods, "The Microwave Spectrum of PO_+: Comparison with SiF^+," *The Journal of Chemical Physics* 94 (1991): 3504.

59. Z. Zhu, C. Cheng, S. Wang, and D. Shi, "Accurate Calculations of the 18 λ-s States and 50 ω States of PO^+ Cation: Potential Energy Curves and Spectroscopic Parameters including the Spin-Orbit Coupling Efifect," *The European Physical Journal D* 68 (2014): 291.

60. X. Tang, G. A. Garcia, J.-F. Gil, and L. Nahon, "Vacuum Upgrade and Enhanced Performances of the Double Imaging Electron/Ion Coincidence End-Station at the Vacuum Ultraviolet Beamline DESIRS," *The Review of Scientific Instruments* 86 (2015): 123108.

61. B. Gans, J. Lievin, P. Halvick, et al., "Single-Photon Ionization of SiC in the Gas Phase: Experimental and Ab Initio Characterization of SiC," *Physical Chemistry Chemical Physics* 25 (2023): 23568.

62. M. Drissi, J.-C. Loison, B. Gans, et al., "VUV Threshold Photoelectron Spectroscopy of Sis," *Physical Chemistry Chemical Physics* 27 (2025): 8121.

63. G. A. Garcia, L. Nahon, and I. Powis, "Two-Dimensional Charged Particle Image Inversion Using a Polar Basis Function Expansion Available," *The Review of Scientific Instruments* 75 (2004): 4989.

64. J. Poully, J. Schermann, N. Nieuwjaer, et al., "Photoionization of 2-Pyridone and 2-Hydroxypyridine," *Physical Chemistry Chemical Physics* 12, no. 14 (2010): 3566–3572.

65. H.-J. Werner, P. J. Knowles, R. Lindh, et al., *MOLPRO, version 2022, a package of ab initio programs*." see http://www.molpro.net.

66. H.-J. Werner and P. J. Knowles, "An Efficient Internally Ontracted Multiconfiguration-Reference Configuration Interaction Method," *The Journal of Chemical Physics* 89 (1988): 5803.

67. E. R. Davidson, "The Iterative Calculation of a Few of the Lowest Eigenvalues and Corresponding Eigenvectors of Large Real-Symmetric Matrices," *Journal of Computational Physics* 17 (1975): 87.

68. H.-J. Werner and P. J. Knowles, "A Second Order Multiconfiguration SCF Procedure with Optimum Convergence," *The Journal of Chemical Physics* 82 (1985): 5053.

69. A. Berning, M. Schweizer, H.-J. Werner, P. J. Knowles, and P. Palmieri, "Spin-Orbit Matrix Elements for Intenrally Contracted Multiconfiguration Interaction Wavefunctions," *Molecular Physics* 98 (2000): 1823.

70. M. J. Frisch, G. W. Trucks, H. B. Schlegel, et al., *Gaussian~16 Revision C.01*. (Gaussian Inc, 2016).

Supporting Information

Additional supporting information can be found online in the Supporting Information section. **Supporting Fig. S1:** Total ion yield for the 63 m/z channel (PS^+). From 7.50 to 8.9 eV a step size of 6 meV was used, while a step size of 100 meV was used for the rest of the spectrum. A zoom of the small step size part is presented in the top-left corner. The sharp peaks observed correspond to autoionization (Rydberg) states of the PS^+. A sharp small rise is observed at 7.90 eV corresponding to the ionization energy. **Supporting Fig. S2:** Intensity colormap of the ionization signal as a function of electron kinetic energy (Ele KE) and photon energy for the 63 m/z channel (PS+). **Supporting Fig. S3:** Energy position (in cm^{-1}) of the vibronic transitions leading to PS^+ electronic ground state ($X\ ^1\Sigma^+$), obtained after fitting the double peaks to a Gaussian function as a function of v'+1/2 (black circles). The red curve corresponds to the fit to a second-degree polynomial function. **Supporting Fig. S4:** Total ion yield as a function of photon energy for the 47 m/z channel (PO+), with two different energy step sizes. From 8.0 to 8.9 eV a step size of 6 meV was used, while a step size of 100 meV was used for the rest of the spectrum. A zoom of the small step size part is presented in the top-left corner. A sharp rise is observed at 8.36 eV corresponding to the ionization energy. **Supporting Fig. S5:** Intensity colormap of the ionization signal as a function of electron kinetic energy (Ele KE) and photon energy for the 47 m/z channel (PO+). **Supporting Fig. S6**: Energy position (in cm^{-1}) of the vibronic transitions to the PO^+ ground electronic state ($X\ ^1\Sigma^+$) as a function of (black circles). Positions are taken as the maximum of the Gaussian functions used to fit each of the three bands. The red curve corresponds to the fit to a second-degree polynomial function. **Supporting Fig. S7:** Potential energy curves of PO and PO^+ calculated at different level of theory. In black, MRCI+Q/V5Z with s and p orbitals in the active space. In red, RCCSD(T)/aug-cc-pwCVQZ. In blue, MRCI+Q/AVTZ with s, p and d orbitals in the active space.